Accepted Manuscript

Estimation of the structure dependent performance of 3-D rapid prototyped membranes

Tim Femmer, Alexander J.C. Kuehne, Matthias Wessling

Estimation of the structure dependent performance of 3-D rapid prototyped membranes

Tim Femmer[a,b], Alexander J.C. Kuehne[b], Matthias Wessling[a,b,*]

[a]*Chemical Process Engineering AVT.CVT, RWTH Aachen University, Turmstraße 46, 52064 Aachen, Germany*
[b]*DWI – Leibniz-Institute for Interactive Materials, RWTH Aachen University, Forckenbeckstraße 50, 52074 Aachen, Germany*

Abstract

Novel rapid prototyping techniques expedite the fabrication of shapes and geometries, which have been inaccessible to date using common machining methods. The attained freedom of design is of paramount importance for advancing membrane science with unprecedented membrane geometries. We investigate such novel shapes and geometries for membranes and compare them to traditional flat-sheet and hollow-fiber architectures. We show a systematical approach towards expedient design by directly evaluating the novel membranes geometries. Previously inaccessible membrane architectures based on triply-periodic minimal-surfaces are manufactured and their performance is assessed using the analogy between heat- and mass transport. This way, we circumvent non-geometrical influences and identify other effects deteriorating membrane performance, for example concentration polarization. The novel membrane geometries outperform flat-sheet and hollow-fiber membrane architectures.

Keywords: Additive manufacturing, rapid prototyping, three-dimensional membrane, minimal surfaces, heat- and mass transport

1. Introduction

In membrane devices, mass transfer and fouling behaviour are decisively governed by the macroscopic geometry of the membrane. Flat-sheet and hollow-fiber geometries are two of the technically most relevant membrane architectures. However, their geometries are the result of available manufacturing possibilities rather than of a performance optimization. Additive production techniques such as rapid prototyping facilitate the generation of nearly any desired shape or structure. However, suitable prototyping resists are rarely applicable for membrane applications. We have recently presented two approaches to generate three-dimensional geometries using photo-lithographic rapid prototyping and PDMS as a membrane material. The first method relies on direct photo-patterning of a PDMS based photoresist,[1] whereas the second approach is based on a sacrificial photoresist, which can be backfilled with nearly any desired membrane material and subsequently removed.[2]

So far, in membrane science only slight and incremental geometry changes have been imposed on traditional membrane geometries to improve mass transport. These changes include for example generation of a micro-structured topology or flow profile engineering. Surface patterning of flat-sheet membranes has been performed using phase separation micro molding,[3–6] thermoforming[7] and curing in structured molds.[8] Multiple flat-sheet membranes can be combined and compacted into space-saving modules by using spacers between the single membrane sheets to improve fluid flow profiles. Different spacer geometries and their effect on mass transfer and fouling have been studied experimentally and numerically.[9–15] Furthermore, multi-layered spacers,[16] membranes with integrated spacers[17, 18] and spacers in tubular membranes[19] have been developed improving membrane performance. The flow-profile of the fluid can also be influenced by macroscopic deformation of the membrane and as a result, curled, twisted and hollow-fibers with complex shapes have been studied and found to enhance mass transfer.[20–27] Such geometries promote mixing and transport phenomena via secondary flows or dean vortices. Innovative fabrication techniques afford non-circular hollow-fiber membranes with topological features on the in- and outside of the membrane.[28–33] Tubular or irregular hollow-fibers can be combined into non-parallel bundles to shape the flow-profile and improve mass transport.[34–37] These studies indicate that the macroscopic membrane geometry and their arrangement is a key factor to improve mass transport and reduce fouling to boost membrane performance.

In view of these developments and the promise of freedom in design held by additive manufacturing techniques, we set out to investigate novel membrane geometries to further advance mass transport, separation and mixing and obtain modules with unprecedented membrane performance.

We investigate sheet-like triply-periodic minimal-surface architectures (TPMS) as an archetype for unprecedented three-dimensional membranes. These sheet-like TPMS structures are composed of two inter-penetrating volume-domains extending in all three dimensions. The two volume-domains are separated by a thin membrane wall[38]. TPMS structures are known for their advanced mechanical properties[39] and are wrinkle-free with a smooth local topology. The smoothness results from a local area minimization principle, which causes the disappearance of mean curvature and Young-Laplace pressure[40].

---

*Phone: +1-49-241-8095488, Fax: +1-49-241-8092252, Manuscripts.cvt@avt.rwth-aachen.de, Turmstraße 46, 52064 Aachen
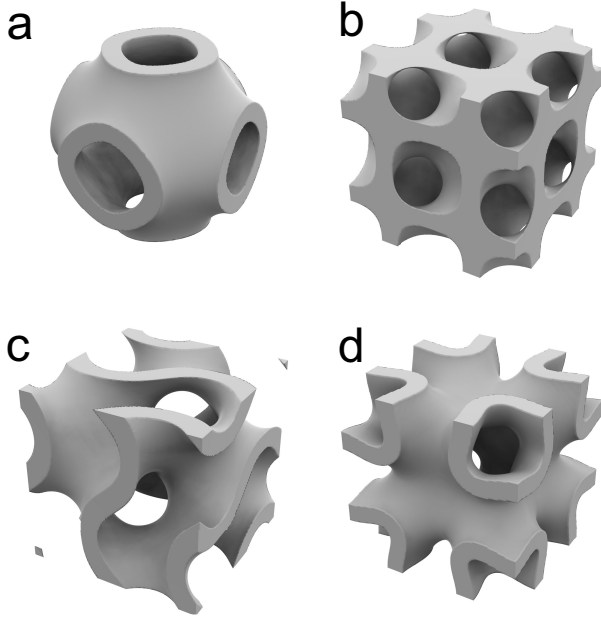
Figure 2: Unit cells of sheet-like TPMS architectures, which serve as heat exchanger walls with a homogeneous thickness separating the two fluid compartments. a) Schwarz-P b) Schwarz-D, c) Schoen-G (Gyroid), d) IWP

This local smoothness should also prevents topology induced fouling[29, 31, 33].

Using the analogy of mass and heat transport, we investigate heat exchange modules to quantify the performance of three-dimensional TPMS geometries and evaluate their transport properties, while excluding interfering non-geometrical effects [41]. We analyze the TPMS geometries by experimentally measuring heat transfer performance as well as by modeling the performance theoretically. Our analysis results in a set of geometry specific heat transfer laws, which can be converted into mass transfer laws, predicting the geometry-specific membrane performance [41].

2. Materials and methods

2.1. Heat exchangers with sheet-like triply-periodic minimal-surfaces architectures

We use a commercially available liquid photo-polymerizable resin WIC100A to prototype the micro heat-exchangers with a commercial digital light processing system (Envisiontec Perfactory P3 Mini Multilense with ERM (1400×1050 pixel)). The resolution is $16 \times 16 \times 25\,\mu m$ in the x-y-z-directions. We prototype micro-heat exchangers (Fig. 1) with a core part consisting of $5 \times 5 \times 5$ TPMS unit cells (Fig. 2). Minimal surface structures are designed using K3dSurf software. The original minimal-surface representation of four different surfaces,[38, 42] namely Schwarz-P, Schwarz-D, Schoen-G, and Schoen-IWP, are approximated by the given equations:[43]

$$\textbf{P:}\ cos(x) + cos(y) + cos(z) = 0$$
$$\textbf{D:}\ cos(x)cos(y)cos(z) - sin(x)sin(y)sin(z) = 0$$
$$\textbf{G:}\ cos(x)sin(y) + cos(y)sin(z) + cos(z)sin(x) = 0$$
$$\textbf{IWP:}\ 2cos(x)cos(y) + 2cos(x)cos(z) +$$
$$2cos(y)cos(z) - cos(2x) - cos(2y) - cos(2z) = 0$$

To create a solid surface wall with a homogeneous thickness, the surfaces facing towards the individual interweaving fluid channels are separated and offset in two directions perpendicular to the surface normal vectors. The offset function and the resulting equations and boundary conditions for the thickened surfaces are given in the Appendix. The surfaces meshes (Fig. 3d3) are scaled-up to $10 \times 10 \times 10\,mm$ and further processed using Rhinoceros CAD software. The step-by-step pathway from the single TPMS unit cell all the way to a rapid prototyped exchanger is shown in Fig. 3. Parameters of the resulting heat-exchanger are summarized in Tab. 1.

2.2. Heat transfer measurements

The experimental setup (Fig. 4) provides hot (50°C) and cold (5°C) milli-Q water with flow rates ($\dot{V}$) between 2 - 25 mL/min, supplied by a rotary piston pump by Ismatec. The milli-Q water is degassed to avoid bubble formation inside the TPMS device. The temperatures (T) are recorded while increasing the flow rates stepwise with each temperature being held for 30 minutes to ensure steady-state heat flux. The transferred heat stream $\dot{Q}$ is averaged between the in- (i) and outlet (o) of the hot (h) and cold (c) fluid streams.

$$\dot{Q} = \frac{\dot{V}\rho}{2}((c_{p,c,o}T_{c,o} - c_{p,c,i}T_{c,i}) + (c_{p,h,i}T_{h,i} - c_{p,h,o}T_{h,o})) \quad (1)$$

with ρ as the liquid density and $c_{p,k,m}$ as the specific heat capacity for the individual water streams. The dimensionless

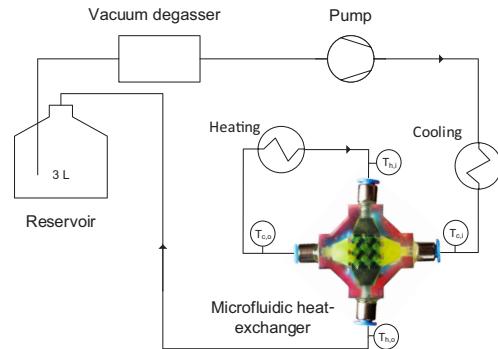Figure 4: Schematic representation of the experimental setup with an illustrative, translucent dummy heat-exchanger of Schoen-G TPMS containing blue and yellow dyed water. Degassed and cooled 5°C water is pumped through the microfluidic heat-exchanger. Subsequently the water stream is heated to 50°C before entering the exchanger on the hot inlet side. Sensors record temperatures at each in- and outlet (Fig. 1a and Fig. 3b3).
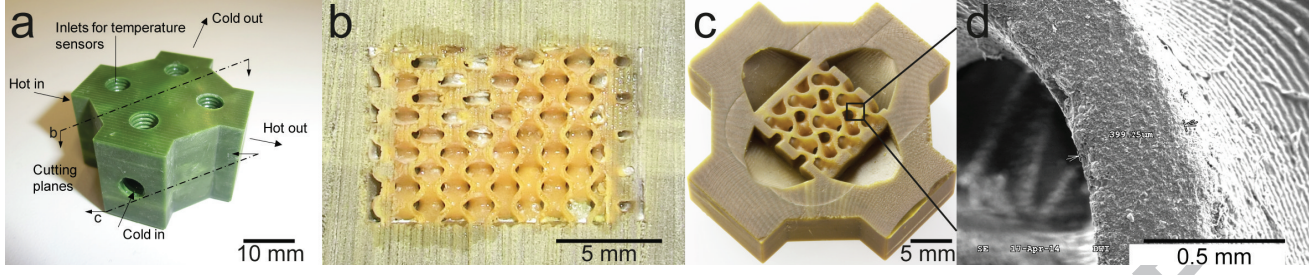
2

Figure 1: a) Prototyped micro heat-exchanger with screw-threaded in- and outlets for quick-connects to tubing and temperature sensors. b) Vertical cross-section through the heat exchanger shows the internal Schwarz-P structure of the core area. c) Horizontal cross section through the core of the Schoen-G exchanger module and d) SEM picture of a horizontal cross section showing wall and staircase-shaped layers as a result of the manufacturing process in the z-direction.

Table 1: Micro heat-exchanger properties: [a]Designed thickness t of separating wall in [mm], [b]exchange area A in the module core, [c]percentage of fluid volume over total volume (fluid + solid), [d]hydraulic diameter of a single fluid channel $\frac{4 \cdot A_c}{P}$ with A_c as the cross section area and P as the wetted perimeter averaged over the channel length and the standard deviation of the hydraulic diameter indicating the change in the fluid flow cross section, [e]length of a geometrically equivalent hollow-fiber. We achieve geometrical equivalence by setting the inner hollow-fiber diameter to the hydraulic diameter of the TPMS, while accounting for the same wall thicknesses and exchange area. [f]Average cross section area of a single fluid channel in the core part of the exchanger module.

Type	Symbol	Wall[a] [mm]	Area[b] [mm²]	Porosity[c] [%]	D_h^d [mm]	L_{hf}^e [mm]	A_c^f [mm²]
P	■	0.4	1145	0.768	1.52±0.68	212	39.6
D	○	0.4	1794	0.625	0.82±0.06	560	31.2
G	□	0.4	1483	0.695	1.05±0.09	378	34.5
IWP	●	0.4	1684	0.652	0.86±0.21	506	32.0

heat transfer effectiveness ϵ describes the rate of the actual heat transfer normalized to the theoretically highest achievable heat transfer rate:

$$\epsilon = \frac{\bar{c}_{p,c}(T_{c,o} - T_{c,i}) + \bar{c}_{p,h}(T_{h,i} - T_{h,o})}{2(c_{p,h,i}T_{h,i} - c_{p,c,i}T_{c,i})} \quad (2)$$

For dimensionless analysis of heat transport, we apply the generalized heat transfer power law:

$$Nu = a \times Re^b \times Pr^{1/3} \quad (3)$$

Parameters a and b are characteristic for the different TPMs structures and the respective transfer regimes. To determine a and b we need to determine the Nusselt, Reynolds and Prandtl numbers. The Reynolds number is determined for each flow rate with the density ρ, dynamic viscosity η, the hydraulic diameter d_h (Tab. 1) and average fluid velocity $v = \dot{V}/A_c$ of the liquid.

$$Re = \frac{\dot{V}}{A_c} \frac{\rho \, d_h}{\eta} \quad (4)$$

The Prandtl number is determined using the dynamic viscosity η, specific heat c_p and thermal conductivity λ_l of the liquid.

$$Pr = \frac{c_p \, \eta}{\lambda_l} \quad (5)$$

Finally, we determine the Nusselt number using the convective heat transfer coefficient α, the length of the cubic heat exchanger inner part $L = 10$ mm and the thermal conductivity of the liquid λ_l following:

$$Nu = \frac{\alpha \, L}{\lambda_l} \quad (6)$$

where α is calculated using the transfer heat stream $\dot{Q} = u \times A \times \Delta T_{ln}$, the logarithmic mean temperature difference ΔT_{ln}, the total exchange area in the core of the exchanger A (Tab. 1) and the overall heat resistance factor u:

$$u = (1/\alpha + t/\lambda_w + 1/\alpha)^{-1} \quad (7)$$

with the thermal conductivity of the rapidly prototyped resist material $\lambda_w = 0.15$ W/(m K) and t as the wall thickness of the heat exchange module.

Having determined the sets of Nu, Re and Pr-numbers for each flow rate, we can derive a and b using Eq. 3.

2.3. Pressure drop evaluation

The apparent pressure drops in the heat exchanger modules are too low to measure them directly. We hence apply CFD simulations using COMSOL Multiphysics to calculate the pressure drops inside the microfluidic heat-exchangers. We compare the coefficients obtained to literature values of straight tubes. The pressure drop coefficient is given as:

$$\zeta = \frac{2 \, \Delta p \, d_h \, \rho}{L \, \dot{V}^2} \quad (8)$$

with Δp as the simulated pressure drop. We fit the pressure drop coefficients to correlations in the form of:
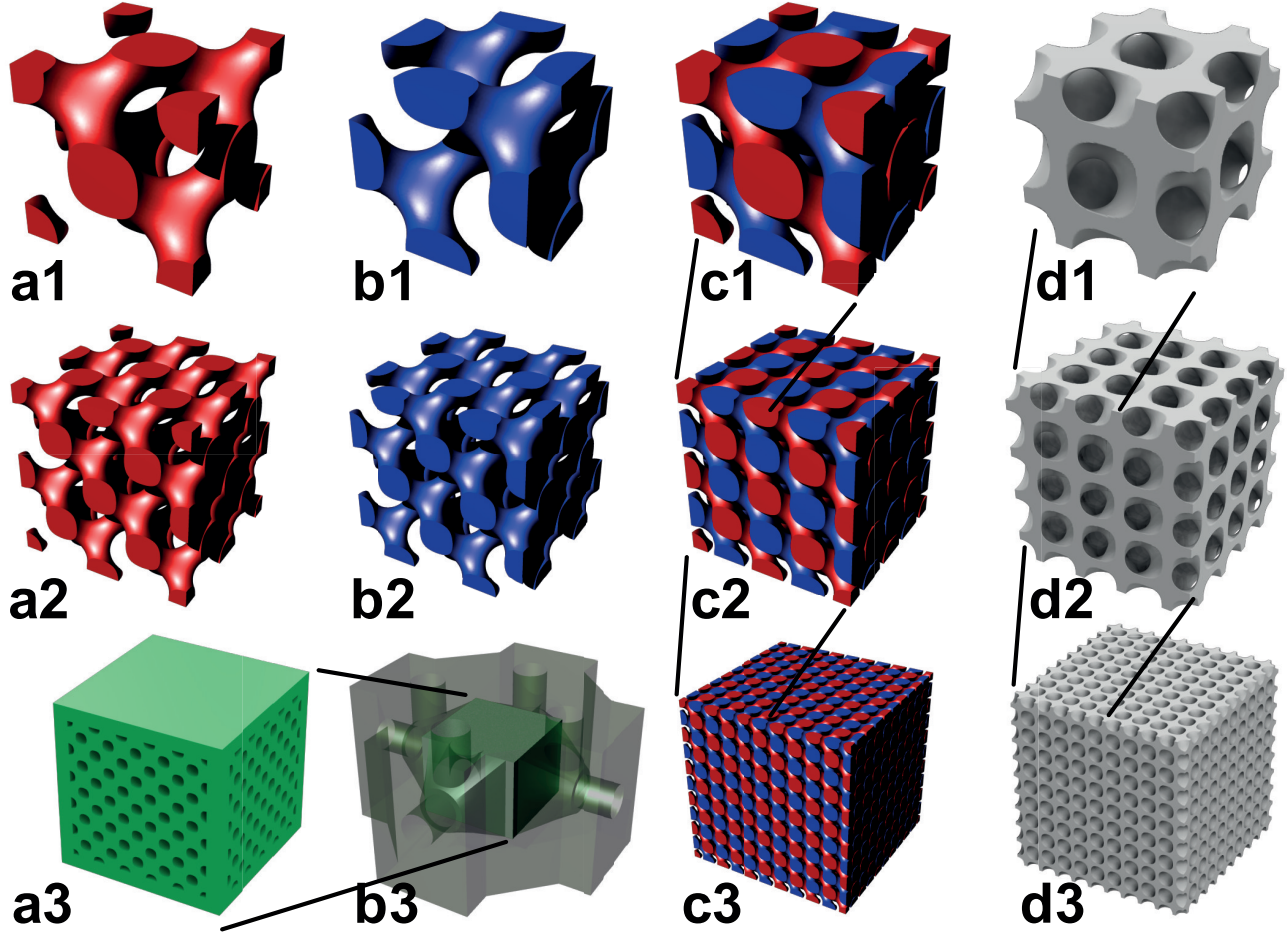
$$\zeta = w/Re \quad (9)$$

3

Figure 3: Process from a single TPMS (Schwarz D) unit cell to a rapidly prototyped micro heat-exchanger with $5 \times 5 \times 5$ unit cells. a1) Unit cell of the hot fluid channel, b1) Unit cell of the cold fluid channel. c1) Assembly of both fluid channels resulting in the negative of d1) representing the unit cell of heat exchanger wall. a2) $2 \times 2 \times 2$ expanded hot fluid channel, b2) exact copy of the hot fluid channel, however offset for the cold fluid, c2) intertwined hot and cold fluid channels from a2) and b2), d2) 8 fold continuous extensions of the sheet like TPMS unit cell, a3) selectively closed fluid channels on the top and bottom of the device to generate a cross-flow module, b3) prototyped exchanger with fluid in- and outlets and connections for temperature sensors, c3) $5 \times 5 \times 5$ extension of the intertwined fluid channels of the TPMS heat exchanger, d3) the backfilled structure of c3) as the geometry being rapidly prototyped, forming the heat transfer interface/wall between the fluid channels.

ζ of a straight tube with laminar flow is 64/Re[44]. Additionally, we determined single channel permeablities by measuring the time until 350 mL of water have passed through the microfluidic heat-exchanger[45]:

$$k = \frac{\eta L}{A_0 M_s} \frac{2 \pi^2 r^4}{(M_0/M_s)^2 - 1} \qquad (10)$$

with $A_0 = 100 \, \text{mm}^2$ as the cross section area of the TPMS heat exchanger core, M_s as the mass flow rate of water through the exchanger in g/s, M_0 as the mass flow rate of water through an exchanger without the TPMS structured core and r as the radius of the outlet tubing. Higher permeabilities through the device correspond to higher flow rates at a lower pressure drop.

For CFD simulations, a single channel of the minimal-surface exchanger is designed using k3dsurf software and exported to Hypermesh 12 software for meshing. We build tetrahedral meshes in the bulk phase with 5 prismatic boundary lay-

ers at the walls. To reduce calculation effort we reduce the core structures into slices of $5 \times 5 \times 1$ unit cells. The total pressure drop is calculated by averaging over twice the pressure drop of the top and bottom slices (one symmetry boundary) and three times the drop of the middle slices (two symmetry boundaries). The flow is corrected accordingly. Each mesh slice consists of 2.9, 3.2, 3.0, 5.5 mio. elements for P, D, G and IWP respectively. We apply laminar in- and outflow boundary conditions with 1 mm entrance length and one fifth of the flow rate. To further quantify the superior performance of our minimal-surface geometries, we compare the pressure drop in the TPMS structures to tubes as a model for hollow-fiber membranes with equal geometry parameters. We achieve geometrical equivalence by setting the inner tube diameter to the hydraulic diameter of the TPMS architectures, while maintaining the wall thickness and exchange interface areas constant. Identical areas are achieved by balancing the inner diameter with the length of the hollow-

4

fiber membrane, as shown in Tab. 1.

3. Results and discussion

3.1. Heat transfer

The heat transfer experiments indicate that the structural membrane performance decreases from Schwarz-D > IWP ~ Schoen-G > Schwarz-P for flow rates above 12 mL/min, as shown in Fig. 5a. The performance scales with the available exchange area, as given in Tab. 1 ($A_D > A_{IWP} > A_G > A_P$). With increasing flow rate ($\dot{V}$ in Eq. 1) the overall transferred heat increases.

To investigate the quality of our devices, we plot their effectiveness of transported heat versus the flow rate, as shown in Fig. 5b. With increasing flow rates the heat transfer effectiveness decreases for all minimal surface exchangers. Increasing the flow rates enhances mixing in the fluid boundary layer and the convective heat transfer coefficient α increases. This should usually lead to higher effectivenesses, however, the residence time in the exchanger overcompensates for the higher convective heat transfer and the overall effectiveness decreases. The effectiveness of Schwarz-P is constant for flow rates above 18 mL/min. Here both effects (rising α but decreasing residence time) balance each other, leading to a moderate effectiveness of 25 % which is also a result of the low thermal heat conductivity of the exchanger wall. Similar to the transferred heat in Fig. 5a the effectiveness of IWP and Schoen-G (Fig. 5c) are nearly identical.

We transform the set of experiments to heat transfer laws (Eq. 3) and compare these with literature values for a flat-sheet membrane $Nu = 0.664 \times Re^{0.5} \times Pr^{1/3}$ and for a straight tube $Nu = 0.664 \times (d_P/L)^{0.5} \times Re^{0.5} \times Pr^{1/3}$[44] with identical hydrodynamic and thermal simulation parameters. For benchmarking of our modules, the membranes are compared to the highest TPMS hydraulic diameter of the Schwarz-P geometry. The dimensionless Nusselt number is plotted versus the Reynolds number, with high Nusselt numbers being desirable. The performance decreases in the order Schwarz-D > Schoen-G > IWP > Schwarz-P for $Re < 15$. The fitted heat transfer laws for each minimal-surface exchanger module are shown in Fig. 5c. With respect to the Reynolds numbers, Schwarz-D transfers the largest amount of heat, followed by the IWP, Schoen-G and Schwarz-P geometries. The heat transfer power laws ($b > 1$) cannot be extrapolated reliably to high Reynolds numbers, as this will surly overestimate the performance for larger Reynolds numbers. Altogether, all minimal-surface heat exchange modules outperform traditional flat-sheet and hollow-tube geometries significantly. The fitted parameters a and b are given in Tab. 2. This performance can be transferred to mass transport in minimal surface membranes. The mass transfer is also improved significantly, compared to hollow-fiber membranes of equal parameter.

3.2. Pressure drop

The enhanced heat transfer in minimal-surface exchangers compared to tubular and flat geometries results in an increased pressure drop. Choosing the right geometry for a specific application always entails a trade-off between the ideal heat transport and the desired pressure drop. The individual pressure drop in a single channel for each minimal-surface architecture is shown in Fig. 6a. The simulated pressure drop rises with the flow rate. The structure-induced laplacian pressure drop from the surface results in an overall small pressure drops below 50 Pa. This proves the high performance of our TPMS geometries for fluid processes and application in heat-exchangers and membrane modules. Although all of the recorded pressure drops are small, the IWP structure exhibits a pressure drop, which is higher than in the Schwarz-D, Schoen-G and about four times higher than in the Schwarz-P geometry. To validate the general trend of the pressure drop simulations we measure the permeability[45] for each TPMS structure according to Eq. 10, as shown in Tab. 2. The permeability describes the fluid flow through an individual channel side of the exchanger. Higher permeabilities indicate a lower pressure drop inside of a given structure. The measurements agree with the simulations giving greater pressure drops for IWP, and lower pressure drops for Schoen-G and Schwarz-P. However, we find a discrepancy for the pressure drop inside the Schwarz-D geometry, which appears to be smaller than in the Schwarz-P geometry, which we believe is the result of inhomogeneities or deviations during the manufacturing process.

We further obtain the pressure drop coefficient ζ (Eq. 8) from the pressure drop simulations for each structure and plot these against the Reynolds number in Fig. 6b. Moreover, we plot the pressure drop coefficient for a straight tube in the same figure and present the derived w-values in Tab. 2. The normalization from flow rate to Reynolds number changes the performance of the TPMS structure. Schoen-G outperforms Schwarz-P, Schwarz-D and IWP (Fig. 6b and w in Tab. 2). Altogether, the TPMS geometries perform very well with an overall range of w between 262 - 426, which is also apparent by the overlapping TPMS curves in Fig. 6b.

3.3. Performance assessment

Our TPMS architectures exhibit pressure drops, which are between four (Schoen-G) and seven times (IWP) higher than in a straight tube, as shown in Fig. 6b and Tab. 2. Although this increased pressure drop impairs the performance of our architectures, the pressure drop results in enhanced heat transfer. To evaluate the trade-off between induced pressure drop and heat transfer we calculate the surface area goodness factor $Nu/(Pr^{1/3} w)$[46–48], which relates the heat transfer to the pressure drop, as shown in Fig. 7a. All TPMS structures outperform a tubular structure except for Schwarz-P, which matches the straight tube in surface area goodness. Moreover, we calculate the ratio of friction per unit of surface area (E) and heat transfer power per unit surface area at a temperature difference of one degree C (h):[46–48]

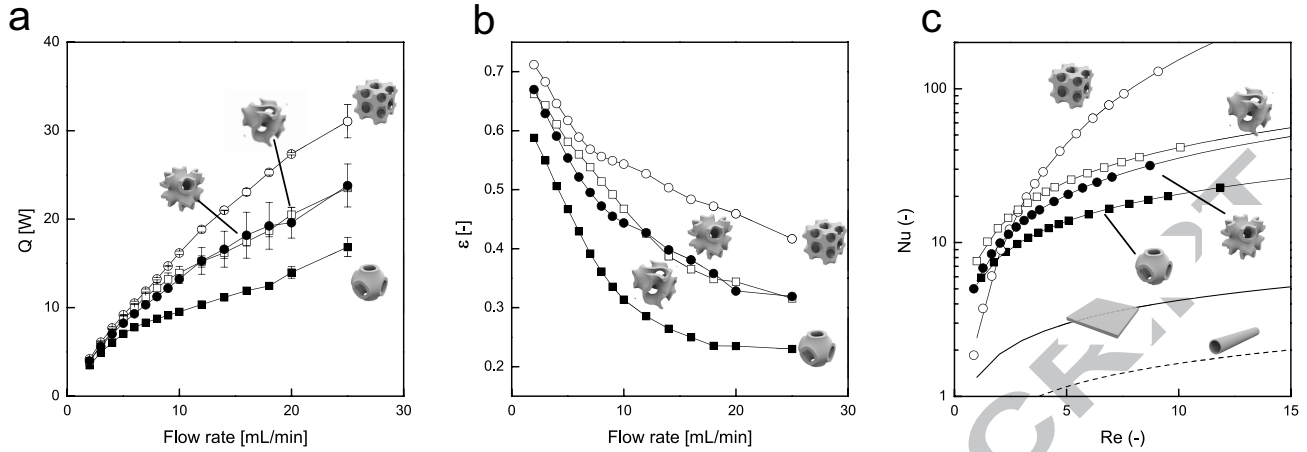$$E = \frac{\Delta p \, \dot{V}}{A} \qquad (11)$$

5

Figure 5: Heat transfer characteristics of four minimal-surface geometries. a) The transferred total heat stream for varying flow rates, b) the heat transfer effectiveness for different flow rates, and c) the fitted heat transfer laws in according to Eq. 4 as obtained from measurements for TPMS heat exchangers together with simulation data obtained for a flat-sheet and a straight tube of comparable geometrical dimensions.

Table 2: Results of heat transfer experiments, pressure drop simulations and permeability measurements. Parameters a and b represent the coefficients for the heat transfer laws of the TPMS structures (Eq. 3). Parameters for flat-sheet and tubular exchangers are taken from literature.[44] The pressure drop coefficient w are derives from Eq. 9 and the single channel permeabilities are derived from Eq. 10.[45]

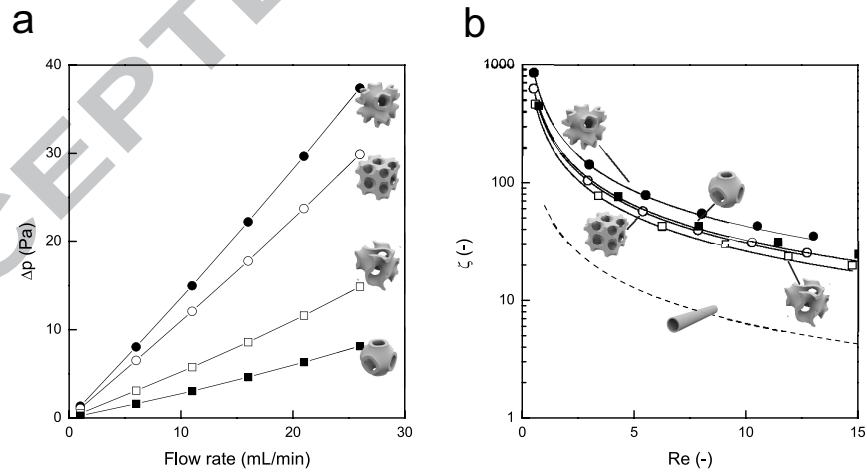| Type	a (-)	b (-)	w (-)	k^a ($10^{-3} \times mm^2$)
P	2.67	0.59	322	3.58
D	1.20	1.81	307	0.88
G	3.79	0.74	262	1.62
IWP	2.81	0.80	426	1.05
Hollow fiber	$0.664\,(\frac{d_h}{L})^{1/2}$	0.5	64	
Flat sheet	0.664	0.5		

Figure 6: Simulation results of single fluid channels for minimal-surface TPMS architectures. a) Pressure drop between in- and outlet versus the liquid flow rate. b) The pressure drop coefficients ζ (Eq. 8) and their fits according to Eq. 9 are plotted versus the Reynolds number for TPMS and tubular structure.

$$h = \frac{Nu\,\lambda_l}{d_h} \qquad (12)$$

The ratio of friction loss E and transferred heat h is plotted over Re in Fig. 7b. We deduce from the fact $E/h << 1$ that the heat
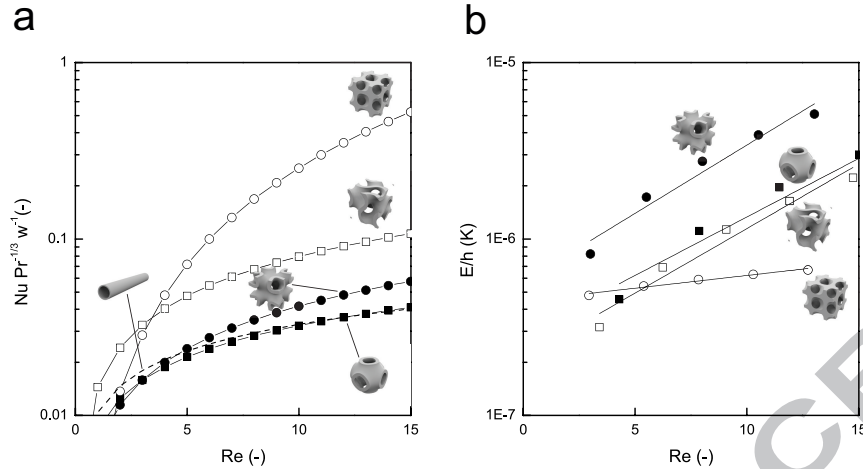
6

Figure 7: Combined evaluation of heat transfer and pressure drop for our TPMS architectures. a) Surface area goodness as a measure for heat transfer in dependence of the induced pressure drop versus *Re*. b) Ratio of friction loss *E* and the transferred heat *h* describing the predominance of the transferred heat in relation to the pressure drop plotted versus *Re*.

transfer dominates the pressure drop despite the low thermal conductivity coefficient of the exchanger module. In agreement with the previous performance assessment, Schwarz-D excels in the ratio of friction to heat transfer as indicated by the small slope in the linear data fits (Fig. 7b).

3.4. Utilization in membrane technology

To transfer our heat exchange results to mass transport and apply these in membrane technology further development are required. On the one hand, rapid prototyping of membranes is required. We successfully showed two fabrication methods for three-dimensional membranes.[1, 2] On the other hand, prove has to be given that the obtained results are valid for mass transport. The analogy between heat and mass transport indicates in theory that the fitting parameters *a* and *b* are equal under certain conditions.[41, 48] Although not all of these conditions are met, we are certain that increased heat transport resolves in better mass transport. Enthalpy exchange which combine heat and moisture transfer proves our assumptions made.
Furthermore with three-dimensional TPMS membranes spacers are not necessary anymore. The potential of TPMS for superior candidates as lightweight material[39] enable pressure resistant membranes modules for revers osmosis or organic solvent nanofiltration. Blut oxygenators benefit from enhanced transport properties and the specific freedom of design in module construction with TPMS membranes based on expandable unit cells. However, rapid prototyping of porous membranes is still a difficult task but the potential of real three-dimensional membranes is high.

4. Conclusions

We report the creation of four rapidly prototyped TPMS heat exchanger geometries together with their performance analysis as candidates for three-dimensional membrane geometries.

Out of the four candidates, Schwarz-D exhibits the best heat transfer characteristics with respect to inherent pressure drop. Compared to hollow-tube and flat-sheet membrane geometries our TPMS modules outperform these by an order of magnitude, showcasing superior heat transport, thus indicating enhanced mass transport when applying these geometries in membrane applications. The mass transport performance of such modules can be modeled using the heat-transfer analogy, as we have shown here, simplifying module characterization and incremental device optimization. We believe that TPMS membranes geometries will most likely perform much better than established here, when beneficial effects such as concentration polarization are taken into account. In the future the presented additive manufacturing technique will allow to further performance of membrane modules impacting on a wide range of technological processes.

Acknowledgement

Nomeclature

a	fitting parameter for heat transfer power law (-)
A	exchange area of TPMS heat exchanger (mm^2)
A_c	average single channel cross section area (mm^2)
A_o	empty cross section of exchanger core (mm^2)
b	fitting parameter for heat transfer power law (-)
c_p	specific heat capacity for water of stream (J kg^{-1} K^{-1})
d_h	hydraulic diameter (mm)
E	friction power per unit of surface area (kg s^{-3})
h	heat transfer power per unit of surface area (W m^{-2} K^{-1})
k	channel permeability (mm^2)
L	length of exchanger (mm)
M_0	mass flow rate of water through exchanger without core part (g s^{-1})
M_s	mass flow rate of water through exchanger with TPMS core part (g s^{-1})
Nu	Nusselt number (-)
Pr	Prandlt number (-)
r	outlet tubing radius (mm)
Re	Reynolds number (-)
T	temperature of water stream (°C)
t	exchanger wall thickness (μm)
u	overall heat transfer resistance (W m^{-2} K^{-1})
$\dot{V}$	flow rate water (mL min^{-1})
w	fitting parameter pressure drop (-)

Greek letters

α	convective heat transfer coefficient (W m^{-2} K^{-1})
ϵ	heat transfer effectiveness (-)
η	dynamic viscosity (kg)
ρ	density water (kg m^{-3})
λ_l	thermal heat conductivity of water (W m^{-1} K^{-1})
λ_w	thermal heat conductivity of exchanger wall (W m^{-1} K^{-1})
ζ	pressure drop coefficient (-)
Δp	pressure difference (mbar)
ΔT_{ln}	logarithmic mean temperature difference (K)

Subscripts

i	inlet
o	outlet
c	cold
h	hot
s	sample

References

References

[1] T. Femmer, A. J. C. Kuehne, M. Wessling, Print your own membrane: Direct rapid prototyping of polydimethylsiloxane, Lab Chip 14 (2014) 2610–2613.

[2] T. Femmer, A. J. Kuehne, J. Torres-Rendon, A. Walther, M. Wessling, Print your membrane: Rapid prototyping of complex 3d-pdms membranes via a sacrificial resist, Journal of Membrane Science.

[3] L. Vogelaar, R. G. H. Lammertink, J. N. Barsema, W. Nijdam, L. A. M. Bolhuis-Versteeg, C. J. M. van Rijn, M. Wessling, Phase separation micromolding: a new generic approach for microstructuring various materials., Small 1 (6) (2005) 645–55.

[4] L. Vogelaar, J. N. N. Barsema, C. J. M. van Rijn, W. Nijdam, M. Wessling, Phase Separation Micromolding - PSμM, Adv. Mater. 15 (16) (2003) 1385–1389.

[5] M. Bikel, P. Z. Culfaz, L. M. Bolhuis-Versteeg, J. G. Perez, R. Lammertink, M. Wessling, Polymeric microsieves via phase separation microfabrication: Process and design optimization, J. Memb. Sci. 347 (1-2) (2010) 93–100.

[6] B. J. Papenburg, L. Vogelaar, L. A. M. Bolhuis-Versteeg, R. G. H. Lammertink, D. Stamatialis, M. Wessling, One-step fabrication of porous micropatterned scaffolds to control cell behavior, Biomaterials 28 (11) (2007) 1998–2009.

[7] R. Truckenmüller, S. Giselbrecht, N. Rivron, E. Gottwald, V. Saile, A. van den Berg, M. Wessling, C. van Blitterswijk, Thermoforming of Film-Based Biomedical Microdevices, Adv. Mater. 23 (11) (2011) 1311–29.

[8] D. A. Vermaas, M. Saakes, K. Nijmeijer, Power generation using profiled membranes in reverse electrodialysis, J. Memb. Sci. 385-386 (2011) 234–242.

[9] C. Fritzmann, M. Hausmann, M. Wiese, M. Wessling, T. Melin, Microstructured spacers for submerged membrane filtration systems, J. Memb. Sci. 446 (2013) 189–200.

[10] L. Liu, L. Li, Z. Ding, R. Ma, Z. Yang, Mass transfer enhancement in coiled hollow fiber membrane modules, J. Memb. Sci. 264 (1-2) (2005) 113–121.

[11] M. Shakaib, S. M. F. Hasani, M. Mahmood, Study on the effects of spacer geometry in membrane feed channels using three-dimensional computational flow modeling, J. Memb. Sci. 297 (1-2) (2007) 74–89.

[12] M. Shakaib, S. M. F. Hasani, M. Mahmood, CFD modeling for flow and mass transfer in spacer-obstructed membrane feed channels, J. Memb. Sci. 326 (2) (2009) 270–284.

[13] A. L. Ahmad, K. K. Lau, M. Z. Abu Bakar, Impact of different spacer filament geometries on concentration polarization control in narrow membrane channel, J. Memb. Sci. 262 (1-2) (2005) 138–152.

[14] G. A. Fimbres-Weihs, D. E. Wiley, Numerical study of mass transfer in three-dimensional spacer-filled narrow channels with steady flow, J. Memb. Sci. 306 (2007) 228–243.

[15] F. Li, W. Meindersma, A. B. de Haan, T. Reith, Optimization of commercial net spacers in spiral wound membrane modules, J. Memb. Sci. 208 (1-2) (2002) 289–302.

[16] J. Balster, I. Punt, D. Stamatialis, M. Wessling, Multi-layer spacer geometries with improved mass transport, J. Memb. Sci. 282 (1-2) (2006) 351–361.

[17] J. Balster, D. Stamatialis, M. Wessling, Towards spacer free electrodialysis, J. Memb. Sci. 341 (1-2) (2009) 131–138.

[18] J. Balster, D. Stamatialis, M. Wessling, Membrane with integrated spacer, J. Memb. Sci. 360 (1-2) (2010) 185–189.

[19] Y. Wu, C. Hua, W. Li, Q. Li, H. Gao, H. Liu, Intensification of micromixing efficiency in a ceramic membrane reactor with turbulence promoter, J. Memb. Sci. 328 (1-2) (2009) 219–227.

[20] J. N. Ghogomu, C. Guigui, J. C. Rouch, M. J. Clifton, P. Aptel, Hollow-fibre membrane module design: comparison of different curved geometries with Dean vortices, J. Memb. Sci. 181 (1) (2001) 71–80.

[21] D. Kaufhold, F. Kopf, C. Wolff, S. Beutel, L. Hilterhaus, M. Hoffmann, T. Scheper, M. Schlüter, A. Liese, Generation of Dean vortices and enhancement of oxygen transfer rates in membrane contactors for different hollow fiber geometries, J. Memb. Sci. 423-424 (2012) 342–347.

[22] S. Liu, Preparation of coiled hollow-fiber membrane and mass transfer performance in membrane extraction, J. Memb. Sci. 215 (1-2) (2003) 203–211.

[23] J. M. Jani, M. Wessling, R. G. H. Lammertink, Geometrical influence on mixing in helical porous membrane microcontactors, J. Memb. Sci. 378 (1-2) (2011) 351–358.

[24] L. Jie, L. Liu, F. Yang, F. Liu, Z. Liu, The configuration and application of helical membrane modules in MBR, J. Memb. Sci. 392-393 (2012) 112–121.

[25] D. N. Kuakuvi, P. Moulin, F. Charbit, Dean vortices: a comparison of woven versus helical and straight hollow fiber membrane modules, J. Memb. Sci. 171 (1) (2000) 59–65.

[26] R. Moll, D. Veyret, F. Charbit, P. Moulin, Dean vortices applied to membrane process, J. Memb. Sci. 288 (1-2) (2007) 321–335.

[27] Z. Borneman, B. Groothuis, M. Willemsen, M. Wessling, Coiled fiber membrane chromatography, J. Memb. Sci. 346 (2) (2010) 327–334.

[28] X. Yang, H. Yu, R. Wang, A. G. Fane, Optimization of microstructured hollow fiber design for membrane distillation applications using CFD modeling, J. Memb. Sci. 421-422 (2012) 258–270.

[29] P. Z. Culfaz, S. Buetehorn, L. Utiu, M. Kueppers, B. Bluemich, T. Melin, M. Wessling, R. G. H. Lammertink, Fouling Behavior of Microstructured Hollow Fiber Membranes in Dead-End Filtrations: Critical Flux Determination and NMR Imaging of Particle Deposition, Langmuir 27 (5) (2011) 1643–1652.

[30] P. Z. Culfaz, E. Rolevink, C. van Rijn, R. G. H. Lammertink, M. Wessling, Microstructured hollow fibers for ultrafiltration, J. Memb. Sci. 347 (1-2) (2010) 32–41.

[31] P. Z. Culfaz, M. Wessling, R. G. H. Lammertink, Fouling behavior of microstructured hollow fiber membranes in submerged and aerated filtrations., Water Res. 45 (4) (2011) 1865–71.

[32] P. Z. Culfaz, M. Wessling, R. Lammertink, Hollow fiber ultrafiltration membranes with microstructured inner skin, J. Memb. Sci. 369 (1-2) (2011) 221–227.

[33] P. Z. Culfaz, M. Haddad, M. Wessling, R. Lammertink, Fouling behavior of microstructured hollow fibers in cross-flow filtrations: Critical flux determination and direct visual observation of particle deposition, J. Memb. Sci. 372 (1-2) (2011) 210–218.

[34] X. Yang, R. Wang, A. G. Fane, Novel designs for improving the performance of hollow fiber membrane distillation modules, J. Memb. Sci. 384 (1-2) (2011) 52–62.

[35] M. M. Teoh, S. Bonyadi, T. S. Chung, Investigation of different hollow fiber module designs for flux enhancement in the membrane distillation process, J. Memb. Sci. 311 (1-2) (2008) 371–379.

[36] S. Buetehorn, L. Utiu, M. Kuppers, B. Blumich, T. Wintgens, M. Wessling, T. Melin, NMR imaging of local cumulative permeate flux and local cake growth in submerged microfiltration processes, J. Memb. Sci. 371 (1-2) (2011) 52–64.

[37] J. Günther, D. Hobbs, C. Albasi, C. Lafforgue, A. Cockx, P. Schmitz, Modeling the effect of packing density on filtration performances in hollow fiber microfiltration module: A spatial study of cake growth, J. Memb. Sci. 389 (2012) 126–136.

[38] E. A. Lord, A. L. Mackay, Periodic minimal surfaces of cubic symmetry, Curr. Sci. i (2003) 346–362.

[39] S. C. Kapfer, S. T. Hyde, K. Mecke, C. H. Arns, G. E. Schröder-Turk, Minimal surface scaffold designs for tissue engineering, Biomaterials (2011) 1–5.

[40] R. T. Armstrong, M. L. Porter, D. Wildenschild, Linking pore-scale interfacial curvature to column-scale capillary pressure, Adv. Water Resour. 46 (2012) 55–62.

[41] E. L. Cussler, Diffusion: Mass Transfer in Fluid Systems, Vol. Second, Cambridge university press, 1997.

[42] A. H. Schoen, Infinite Periodic Minimal Surfaces without self-intersections, NASA Tech. Note.

[43] P. Gandy, Nodal surface approximations to the P, G, D and I-WP triply periodic minimal surfaces, Chem. Phys. Lett. 336 (3-4) (2001) 187–195.

[44] V. D. Ingenieure, VDI-Waermeatlas, Springer-Verlag Berlin Heidelberg, 2006.

[45] J. M. Kemppainen, Mechanically stable solid freeform fabricated scaffolds with permability optimized for cartilage tissue engineering, Ph.D. thesis, University of Michigan (2008).

[46] R. K. Shah, D. P. Sekulić, Fundamentals of Heat Exchanger Design, Wiley, Hoboken, 2003.

[47] W. M. Kays, M. E. Crawford, Convective Heat and Mass Transfer, McGraw Hill, 1987.

[48] W. M. Kays, A. L. London, Compact Heat Exchangers, Krieger Publishing Company, 1998.

Offset function

with t as offset distance parameter, which is adjusted to generate 400 μm thick heat exchanger wall.

$$F_{\text{offset}}(x, y, z) = F(x - a_x, y - a_y, z - a_z) \cdot F(x + a_x, y + a_y, z + a_z)$$

$$a_x = \frac{t}{j} \cdot \frac{\partial F()}{\partial x}; a_y = \frac{t}{j} \cdot \frac{\partial F()}{\partial y}; a_z = \frac{t}{j} \cdot \frac{\partial F()}{\partial z}$$

$$j = \sqrt{\left(\frac{\partial F()}{\partial x}\right) + \left(\frac{\partial F()}{\partial y}\right) + \left(\frac{\partial F()}{\partial z}\right)}$$

Appendix to:

Estimation of the structure dependent performance of 3-D rapid prototyped membranes

Tim Femmer[a,b], Alexander J.C. Kuehne[b], Matthias Wessling[a,b,]

[a]*Chemical Process Engineering AVT.CVT, RWTH Aachen University, Turmstraße 46, 52064 Aachen, Germany*
[b]*DWI – Leibniz-Institute for Interactive Materials, RWTH Aachen University, Forckenbeckstraße 50, 52074 Aachen, Germany*

Offset function

$$F_{\text{offset}}(x, y, z) = F(x - a_x, y - a_y, z - a_z) \cdot F(x + a_x, y + a_y, z + a_z)$$

$$a_x = \frac{t}{j} \cdot \frac{\partial F()}{\partial x}; a_y = \frac{t}{j} \cdot \frac{\partial F()}{\partial y}; a_z = \frac{t}{j} \cdot \frac{\partial F()}{\partial z}$$

$$j = \sqrt{\left(\frac{\partial F()}{\partial x}\right) + \left(\frac{\partial F()}{\partial y}\right) + \left(\frac{\partial F()}{\partial z}\right)}$$

with *t* as offset distance parameter, which is adjusted to generate
400 μm thick heat exchanger wall.

- Rapid prototyping of novel performance structures.
- Fabrication of 3D-triple periodic minimal surfaces.
- Systematic structure evaluation.
- Analogy between heat and mass transport.
- Superior structures for heat and mass transport.